nature physics

Article

https://doi.org/10.1038/s41567-025-03002-8

Universal quantum gate set for Gottesman–Kitaev–Preskill logical qubits

Received: 19 December 2024

Accepted: 16 July 2025

Published online: 21 August 2025

Check for updates

V. G. Matsos[1,2] ✉, C. H. Valahu[1,2,3], M. J. Millican[1,2], T. Navickas[1,2,4], X. C. Kolesnikow[1,2], M. J. Biercuk[1,2] & T. R. Tan[1,2,3] ✉

Conventional approaches towards creating a large-scale, fault-tolerant quantum computer require an error correction scheme that uses multiple physical qubits to encode one logical qubit of protected quantum information. A key limiting factor in realizing error-corrected quantum information processing is the large ratio of physical-to-logical qubits required by many error correction codes, outstripping the size of near-term devices. The Gottesman–Kitaev–Preskill (GKP) code offers hardware efficiency at the cost of increased encoding complexity by encoding a logical qubit into a single quantum harmonic oscillator. Building on earlier demonstrations of GKP-encoded operations, we realize an entangling gate on GKP logical qubits. Our experiments use an optimal control strategy that deterministically implements a universal set of energy-preserving logical gates on finite-energy GKP states encoded in the mechanical motions of a trapped ion. We also directly generate a GKP Bell state starting from vacuum. Our approach is compatible with existing hardware architectures, demonstrating the potential for optimal control techniques with advanced encoding schemes to accelerate the path towards large-scale fault-tolerant quantum information processing.

Using bosons for quantum information processing (QIP) is a promising pathway to accelerate the realization of scaled quantum computers to solve practical problems in quantum chemistry, material designs and secured communications, among others. Bosonic quantum computing leverages the infinite-dimensional Hilbert spaces of harmonic oscillators to encode error-correctable logical qubits[1,2]. This encoding strategy can be implemented on existing devices without the need for substantial physical redundancy, offering a hardware-efficient avenue for fault-tolerant QIP. Among the various bosonic error correction schemes that have been proposed[3–5], the Gottesman–Kitaev–Preskill (GKP) encoding[6] provides in-principle superior error correction performance against dominant hardware decoherence channels[7]. This, coupled with the relative ease of implementing Pauli and stabilizer operations, has made it an attractive option for realizing bosonic error correction across various physical platforms, including electromagnetic modes in microwave cavities[8–12], optical photons[13], and in the mechanical oscillation of trapped ions[14–16]. Recent years have seen substantial progress in this area, including using dissipative[12,15] and measurement-based[8,10] error correction to stabilize GKP code words. However, a key outstanding requirement for universal GKP QIP—a universal gate set for GKP codes—remains elusive.

This challenge arises for two primary reasons. The first is the difficulty of engineering high-quality controls to realize an entangling interaction between bosonic modes. Second, complications due to physically realizable GKP states require careful consideration as they diverge from idealizations[17]. Ideal GKP states are unphysical due to their infinite energy. They are made physical by applying a damping envelope, typically a Gaussian profile, that bounds the energy (Fig. 1a,b). Crucially, applying logical operations designed for ideal GKP states to physical GKP code words distorts the Gaussian envelope and causes errors. Although these errors may be corrected, they require additional rounds of error correction. Several proposals aim to reduce

[1]School of Physics, University of Sydney, Sydney, New South Wales, Australia. [2]ARC Centre of Excellence for Engineered Quantum Systems, University of Sydney, Sydney, New South Wales, Australia. [3]Sydney Nano Institute, University of Sydney, Sydney, New South Wales, Australia. [4]Present address: Q-CTRL, Sydney, New South Wales, Australia. ✉e-mail: vassili.matsos@sydney.edu.au; tingrei.tan@sydney.edu.au

https://doi.org/10.1038/s41567-025-03002-8

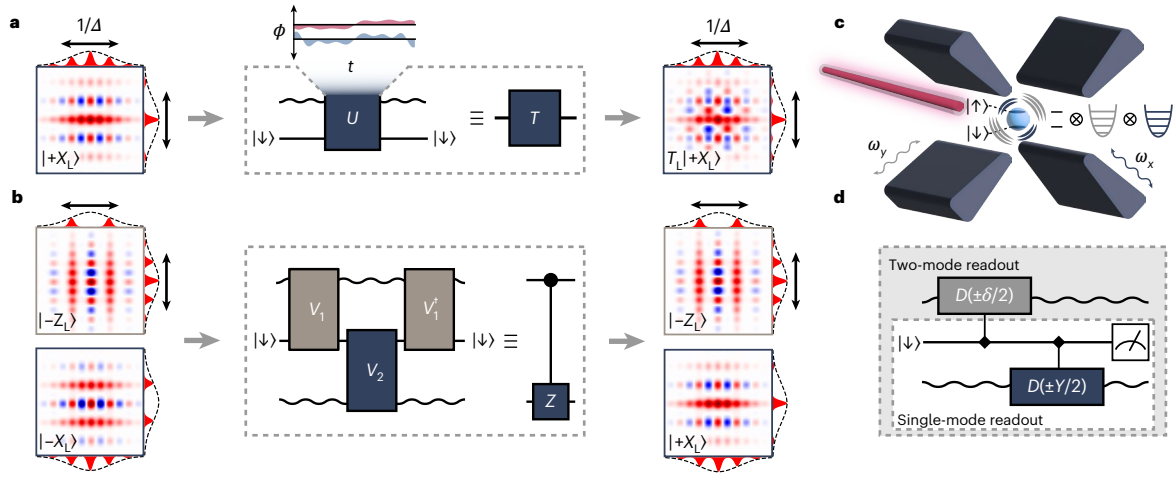

Fig. 1 | Implementation of a universal gate set in an ion trap with logical GKP states. a, SQ gates are implemented with a unitary operation, $\hat{U}$. An example of a $\hat{T}_L$ gate acting on a $|+X_L\rangle$ initial GKP state is shown. The Wigner functions of the initial and final GKP states are plotted. **b**, A TQ CZ_L gate is implemented with a sequence of three sequential unitary operations, namely, $\hat{V}_1$, $\hat{V}_2$ and $\hat{V}_1^\dagger$. In both quantum circuits, the unitary operations comprising the logical SQ and TQ gates act on both spin (straight line) and bosonic (wavy line) modes, and are obtained from a numerically optimized phase modulation of the SDF interaction (inset of $\hat{U}$ in **a**). All gates are deterministic and preserve the finite-energy envelope of physical GKP states, which can be seen from the preservation of the envelope of the final state. The envelope is characterized by the envelope parameter, Δ. **c**, Logical GKP states are encoded in a single trapped ion's radial-x and radial-y motional modes. A pair of radio-frequency and d.c. electrodes generate the two radial harmonic potentials with frequencies $\{\omega_x, \omega_y\} = 2\pi \times \{1.33, 1.51\}$ MHz. Laser interactions induce SDFs that couple the ancillary spin and motion. **d**, Single- or two-mode measurement of logical GKP Pauli expectation values. The measurement is obtained by spin readout in the $\hat{\sigma}_z$ basis after applying displacements conditioned on the ancilla state in the $\hat{\sigma}_x$ basis (black diamond). The logical Pauli measurement is chosen by the complex values of the displacements, γ and δ.

this overhead[9,17–19], but experimental demonstration has been limited to single-qubit (SQ) operations through a dissipative strategy[15].

Here we demonstrate the first realization of a universal logical gate set for GKP qubits. Our gate set is coherent, deterministic and designed to avoid code word distortion of finite-energy GKP states. The key enabler of our approach is an optimal control strategy that implements a highly tunable temporal modulation of a spin–boson interaction. This interaction couples a high-quality ancillary two-level spin and two bosonic modes of a trapped ion (Fig. 1 shows a visual summary). The spin's excellent coherence properties enable it to function as a nonlinear element for implementing logical GKP operations, and as a mediator of bosonic entanglement with minimal decoherence. We implement a gate set composed of the SQ gates $\{\hat{R}_L^X(-\pi/2), \hat{R}_L^Z(-\pi/2), \hat{T}_L = \hat{R}_L^Z(\pi/4)\}$ and the two-qubit (TQ) controlled-Z (CZ_L) gate, which contains all necessary operations for universal quantum computation[20,21]. We also demonstrate the preparation of a GKP Bell state from vacuum in a single step, providing an alternative route to universality[22]. We perform logical quantum process tomography (QPT) and logical quantum state tomography (QST) to characterize the logical gate set and the Bell state, and we discuss strategies to mitigate identified error sources.

We perform experiments with a single $^{171}Yb^+$ ion confined in a room-temperature Paul trap with favourable coherence in both the ancillary qubit and the bosonic modes (ref. 23 provides details on the experimental setup). The ancillary qubit has a measured T_2^* coherence time of 8.7 s (ref. 24); the motional coherence time of an equal superposition of the Fock states, $|0\rangle$ and $|1\rangle$, is measured as ~50 ms (ref. 16); and the heating rate is 0.2 quanta per second. Coherent phase-modulated spin–motion interactions are implemented by a 355-nm pulsed laser through stimulated Raman transitions.

The control required to prepare and manipulate approximate GKP code words is provided by laser-driven state-dependent forces (SDFs) with the Hamiltonian described by[25]

$$\hat{H}_j^{\mathrm{SDF}}(t) = \frac{\Omega_j}{2}\hat{\sigma}_{\phi_s(t)}\left(\hat{a}_j^\dagger e^{-i\phi_m(t)} + \hat{a}_j e^{i\phi_m(t)}\right), \quad (1)$$

where $\Omega_j = 2\pi \times 2.4$ kHz is the Rabi rate on bosonic mode j, with annihilation operator $\hat{a}_j$; ϕ_s and ϕ_m are independently controllable phases associated with the spin and bosonic modes, respectively. The operator $\hat{\sigma}_{\phi_s(t)} = \hat{\sigma}_x \cos\phi_s(t) + \hat{\sigma}_y \sin\phi_s(t)$ is expressed in terms of Pauli matrices $\hat{\sigma}_x, \hat{\sigma}_y$ that act on the spin state of the ion. The non-commutativity of the modulated SDF interaction provides the requisite nonlinearity to prepare and control the GKP states[16]. Alternating the SDF interactions between two bosonic modes (Fig. 1b) enables entangling operations between them[26]. We achieve state preparation and logical operations exclusively through the modulation of the phases $\phi_s(t)$ and $\phi_m(t)$ in $\hat{H}_j^{\mathrm{SDF}}(t)$. The waveforms for these modulations are numerically optimized[27]. The constructed pulses are designed to prevent distortions of the physical code words. Specifically, the cost function for both SQ and TQ gates minimizes the average error that maps a set of finite-energy input states to the target corresponding output states[9]. The cost function for preparing the Bell state minimizes the state overlap infidelity with respect to the target finite-energy state. The result of these optimizations is a library of waveforms that can be sequenced to enact the desired quantum circuit.

In the first experiment, we implement and fully characterize a logical SQ gate set. The experimental sequence consists of three steps: state preparation, gate application and logical readout. State preparation creates GKP states from vacuum in the radial-x motional mode using a similar optimized state preparation protocol[16], augmented to suppress previously neglected errors from higher-order Hamiltonian terms. Numerically optimized waveforms are independently generated to prepare different approximate logical GKP states, including $|+X_L\rangle$, $|+Y_L\rangle$, $|+Z_L\rangle$ and $|-Z_L\rangle$, with durations between 651 µs and 821 µs. The approximate nature of the states is parameterized through their envelope parameter Δ, and the ideal GKP states are retrieved in the limit of infinite squeezing (Methods). Our prepared states have a target envelope parameter between 7.9 dB and 8.9 dB. During gate application, $\hat{H}_x^{\mathrm{SDF}}(t)$ is applied with the waveform corresponding to the desired gate, with durations ranging from 196 µs to 339 µs. Mid-circuit measurements are performed after state preparation and gate application to remove residual spin–boson entanglement

https://doi.org/10.1038/s41567-025-03002-8

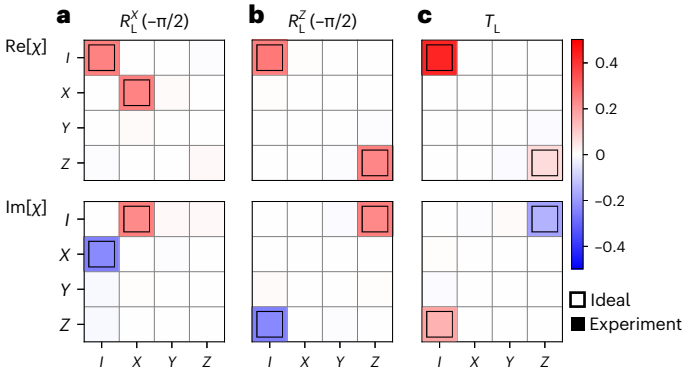

Fig. 2 | QPT of SQ gates. a–c, Real (top) and imaginary (bottom) parts of the χ matrix obtained from QPT shown for the $\hat{R}_L^X(-\pi/2)$ (**a**), $\hat{R}_L^Z(-\pi/2)$ (**b**) and $\hat{T}_L = \hat{R}_L^Z(\pi/4)$ (**c**) gates. The non-zero values of the ideal χ matrix, χ_{id}, are represented by thick coloured borders around the experimental data. From the experimental χ matrices, we obtain logical process fidelities of $\bar{\mathcal{F}}_{proc.} = \{0.94, 0.96, 0.96\}$ and logical average gate fidelities of $\bar{\mathcal{F}}_{gate} = \{0.94(2), 0.96(2), 0.95(2)\}$, where the uncertainties are obtained from a bootstrapping analysis of the experimental χ matrices (Methods). The fidelity is primarily limited by motional dephasing. The ideal unitary operations, $\hat{U}$, yield average gate fidelities, $\mathcal{F}_{gate} > 0.998$, limited by pulse-design imperfections (Supplementary Section A).

(Supplementary Fig. 4). Additionally, the experiment only proceeds when the spin is determined to be in $|\downarrow\rangle$ via projective measurement. Logical readout is achieved by applying an SDF pulse that transfers logical information from the GKP state to the ancilla, which is then measured using state-dependent fluorescence (Fig. 1d). This measurement probes the real part of the expectation value of a displacement operator, $\mathrm{Re}\langle\hat{D}(\gamma)\rangle$, where $\hat{D}(\gamma) = e^{\gamma\hat{a}^\dagger - \gamma^*\hat{a}}$ denotes the bosonic displacement operator.

The experimental sequence outlined above describes one step of a QPT routine on the logical SQ gates. By preparing a range of input states and decoding the input and corresponding output states, QPT characterizes a completely positive trace-preserving map, $\mathcal{E}$. This mapping relates the reconstructed logical input and output states as $\hat{\rho}_L^{out} = \mathcal{E}(\hat{\rho}_L^{in}) = \sum_{m,n}\chi_{m,n}\hat{E}_m\hat{\rho}_L^{in}\hat{E}_n^\dagger$, where $\hat{E}_m$ are the standard Pauli operators, forming the operator basis for the logical Hilbert space. The complex matrix χ fully describes $\mathcal{E}$ and determines the logical process fidelity, $\bar{\mathcal{F}}_{proc.} = \mathrm{Tr}(\chi\chi_{id})$, where χ_{id} describes the ideal transformation associated with the target gate on two-level systems. Furthermore, we relate $\bar{\mathcal{F}}_{proc.}$ to the logical average gate fidelity[28], $\bar{\mathcal{F}}_{gate} = \frac{d\bar{\mathcal{F}}_{proc.}+1}{d+1}$, where d is the dimension of the logical Hilbert space, to quantify the fidelity of the gate averaged over all pure logical input states. For all operations presented, we also simulate the ideal unitary evolutions corresponding to the designed control pulses, which act on the full joint Hilbert space of the spin and bosonic mode(s). All operations achieve near-unity average gate fidelities, $\mathcal{F}_{gate}$, in the absence of decoherence (Supplementary Section A).

We use the stabilizer subsystem decomposition (SSSD) formalism[29] to efficiently retrieve the logical information contained in the finite-energy GKP qubits. This approach addresses the shortcomings of measuring finite-energy GKP states via the conventional usage of the logical Pauli operators, $\{\langle\hat{X}_L\rangle, \langle\hat{Y}_L\rangle, \langle\hat{Z}_L\rangle\}$. The SSSD may be used to provide a more accurate fidelity estimate by measuring the expectation value of logical Pauli measurement operators (henceforth referred to as Pauli measurement operators for brevity), namely, $\{\langle\hat{X}_m\rangle, \langle\hat{Y}_m\rangle, \langle\hat{Z}_m\rangle\}$. Each expectation value of the Pauli measurement operators is obtained by a weighted sum of displacements on the GKP lattice (Methods)[30]. In practice, the truncation of this sum can be chosen to obtain adequate accuracy of fidelity. The reconstructed χ matrices obtained from QPT through SSSD for the SQ gate set $\{\hat{R}_L^X(-\pi/2), \hat{R}_L^Z(-\pi/2), \hat{T}_L = \hat{R}_L^Z(\pi/4)\}$ are shown in Fig. 2. From this, we compute $\bar{\mathcal{F}}_{gate} = \{0.94(2), 0.96(2), 0.95(2)\}$.

In the second experiment, we implement and characterize a TQ CZ_L entangling gate by interleaving SDF interactions between bosonic modes. In particular, the CZ_L gate is decomposed into three sequential unitary operations, $\hat{U}_{CZ} = \hat{V}_1^\dagger\hat{V}_2\hat{V}_1$ (Fig. 1b), each involving a single bosonic mode, leading to a total gate duration of 993 µs; $\hat{V}_1$ and $\hat{V}_2$ are generated by applying $\hat{H}_y^{SDF}$ and $\hat{H}_x^{SDF}$, respectively. Decomposing the CZ_L operation into three individual spin–boson interactions offers two notable advantages: first, this reduces the complexity of the experimental implementation by requiring fewer calibration steps; second, it increases the computational efficiency of the control waveform design, since expensive tasks in numerical optimization need to only consider a reduced Hilbert space. Computational efficiency is further increased by constraining the first and third unitary operations to be inverse of one another.

We characterize the TQ CZ_L gate using QPT to reconstruct the χ matrix and determine the process fidelity. The experimental sequence follows the general structure of the SQ experiment. First, state

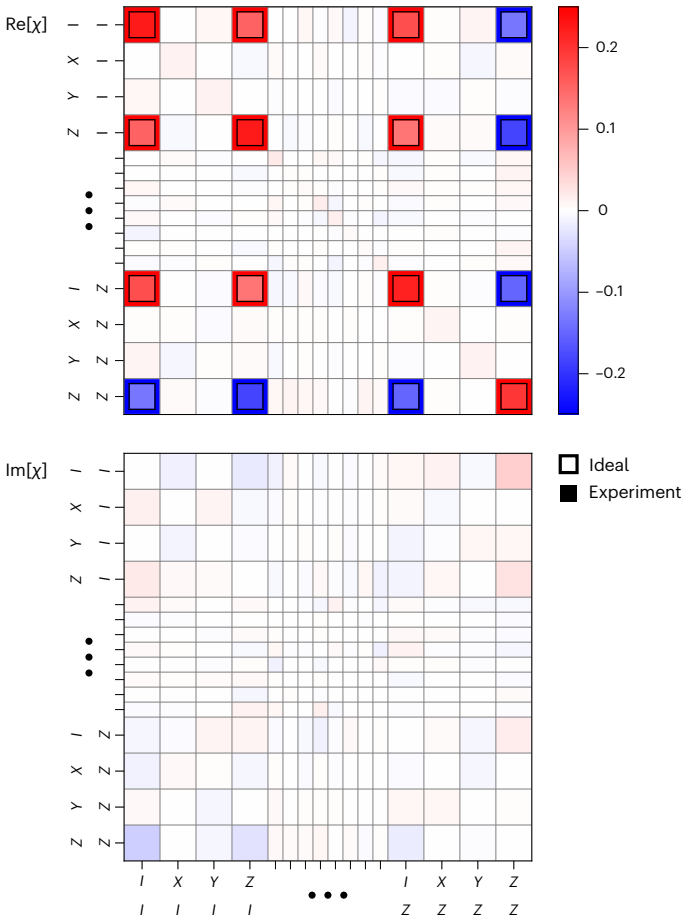

Fig. 3 | QPT of a TQ logical entangling gate. The real (top) and imaginary (bottom) parts of the χ matrix obtained from QPT are shown for the CZ_L gate. The non-zero values of the ideal χ matrix, χ_{id}, are represented by thick coloured borders around the experimental data. Elements of the χ matrix that are near zero are plotted with smaller rows and columns, and the omitted labels (···) are $\{IX, XX, YX, ZX, IY, XY, YY, ZY\}$. The imaginary part of the experimental χ matrix is small, in agreement with the vanishing ideal matrix elements of χ_{id}. We determine a logical process fidelity of $\bar{\mathcal{F}}_{proc.} = 0.68$ and a logical average gate fidelity $\bar{\mathcal{F}}_{gate} = 0.73(1)$, with the gate error dominated by motional dephasing. The ideal unitary operation, $\hat{U}_{CZ}$, yields an average gate fidelity $\mathcal{F}_{gate} = 0.990$, limited by pulse-design imperfections (Supplementary Section A).

https://doi.org/10.1038/s41567-025-03002-8

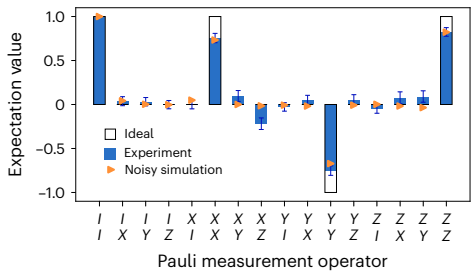

Fig. 4 | QST of a maximally entangled GKP logical Bell state. The Bell state $|\Phi_L^+\rangle = (|+Z_L, +Z_L\rangle + |-Z_L, -Z_L\rangle)/\sqrt{2}$ is prepared from vacuum using an optimized control pulse. Experimental data (shaded bars) are the expectation values of Pauli measurement operators obtained from QST, with the centre representing the mean and vertical error bars indicating the standard deviation ($\pm 1\sigma$) computed from a distribution of 1,000 bootstrapped reconstructions. Black bars represent the corresponding expectation values of an ideal Bell state in two-level systems. We determine a logical state fidelity of $\bar{\mathcal{F}} = 0.83(3)$. Orange triangles are obtained from numerical simulations of the experimental pulse sequence with motional dephasing. The results correspond to a logical state fidelity of $\bar{\mathcal{F}} = 0.81$ and are in agreement with the experimental data. The experiment does not measure $\langle \hat{I}_m \hat{I}_m \rangle$, which is set to 1. The ideal unitary operation, $\hat{U}_{\text{Bell}}$, prepares a logical Bell state with a state fidelity of $\mathcal{F} = 0.984$ (Supplementary Section A).

preparation uses numerically optimized preparation waveforms to sequentially initialize GKP states in the radial-y and radial-x modes. Gate application implements the CZ_L operation by sequentially applying modulated SDF pulses, as described above. Logical readout uses two sequential SDF pulses to transfer information from both bosonic modes to the ancilla (Fig. 1d). This allows the simultaneous measurement of both modes of the form $\text{Re}\langle \hat{D}(\gamma) \otimes \hat{D}(\delta) \rangle$. Setting γ and δ to points on the GKP square lattice results in joint expectation values of the logical Pauli operators (for example, $\langle \hat{X}_L \otimes \hat{Z}_L \rangle$), which inform the χ matrix calculation. Here we only measure the expectation value of the logical Pauli operators instead of the Pauli measurement operators to reduce the total number of required measurements. This introduces a non-negligible error that we discuss below. The reconstructed χ matrix for CZ_L is shown in Fig. 3. From this, we extract a logical average gate fidelity of $\bar{\mathcal{F}}_{\text{gate}} = 0.73(1)$. The experimental and ideal χ matrices show good qualitative agreement: the dominant elements of the matrix are real and are located in the Pauli basis labels $\{II, ZI, IZ, ZZ\}$, and the imaginary part of the experimental χ matrix remains near zero. The infidelity is due to known experimental errors, described below.

In the third experiment, we directly prepare a GKP Bell state from vacuum in a single step, representing an efficient method for GKP resource state synthesis[31]. This direct preparation removes the usual overhead of state preparation followed by an entangling gate to generate a Bell state. We prepare the logical Bell state, $|\Phi_L^+\rangle = (|+Z_L, +Z_L\rangle + |-Z_L, -Z_L\rangle)/\sqrt{2}$, from the initial ground state, $|\downarrow, 0, 0\rangle$. Similar to CZ_L, the unitary operation $\hat{U}_{\text{Bell}}$ is constructed with three numerically optimized unitary operations applied in sequence, $\hat{U}_{\text{Bell}} = \hat{W}_3 \hat{W}_2 \hat{W}_1$, with a total duration of 1.86 ms.

The Bell state is characterized using QST by measuring the two-mode Pauli measurement operators, for example, $\langle \hat{X}_m \otimes \hat{Z}_m \rangle$. Experimental expectation values of these operators are shown in Fig. 4. These measurements are used to construct a logical density matrix, $\hat{\rho}_{\text{L,Bell}}$, which contains the logical information encoded in the state (Methods). Performing logical state tomography through the SSSD in this way requires a vastly reduced set of measurements compared with the number of measurements required to perform full state tomography for a two-mode bosonic state. We determine a logical state fidelity[32], $\bar{\mathcal{F}} = \langle \Phi^+ | \hat{\rho}_{\text{L,Bell}} | \Phi^+ \rangle$, of 0.83(3).

The investigation of the impact of various noise mechanisms in our experiment reveals that the dominant error source is motional dephasing originating from fast fluctuations in the trapping potential. The CZ_L experiment also suffers from non-negligible logical readout error due to measurements of logical Pauli operators on finite-energy states; this accounts for approximately one-fifth of the total error. This can be mitigated by measuring the Pauli measurement operators at the cost of more experimental measurements. In the Bell state experiment, the state fidelity suffers additional errors from thermal noise due to imperfect bosonic ground state initialization. A comprehensive analysis of the dominant errors is given in Supplementary Section C.

In summary, we demonstrated a universal gate set and direct Bell state generation for finite-energy GKP qubits. Our approach uses dynamically modulated light-atom interactions to implement coherent operations that are made to preserve the finite-energy envelope of GKP code words. These control pulses take advantage of the excellent coherence properties of the spin present in the trapped-ion system, which serves as a resource-efficient nonlinear element to enable high controllability and as a high-quality mediator of bosonic entanglement. We characterized these operations with an efficient multimode logical tomography procedure tailored for finite-energy GKP qubits.

We identified straightforward hardware improvements to suppress infidelities. Motional dephasing errors can be mitigated by reducing the dissipative rate in the hardware and increasing the speed of state preparation and logical gates. A faster speed can be achieved by increasing our light-atom coupling strength, Ω_j, which is modest compared with state-of-the-art trapped-ion platforms[33]. We estimate, through numerical simulation, that a ten times improvement of the coupling strength and increasing the motional coherence time to 200 ms suppress the dephasing error to below 3×10^{-3} across all experiments. Similarly, bosonic thermal noise can be suppressed by improving the bosonic mode initialization protocol[34].

Looking forward, our demonstration of a universal gate set on GKP qubits provides a foundation to enable large-scale QIP with bosonic resources on trapped-ion devices. The control methods developed here are compatible with a range of existing hardware. These include linear Coulomb crystals[35,36], two-dimensional ion arrays[37–40], quantum charge-coupled devices[25,41] and micro-Penning traps[42]. These methods can also be extended to the manipulation of motional modes in neutral atoms trapped in optical tweezers[43]. Recent experimental advances motivate further exploration of scalable bosonic QIP in trapped-ion systems. Following the demonstration of a protected-mode encoding to mitigate measurement-induced heating in a quantum charge-coupled device trap[44], a promising direction is to integrate universal control and quantum error correction with the non-destructive measurements of bosonic modes. Additionally, our control facilitates scaling across multiple trapping zones in distributed architectures, leveraging photon interconnects and spin–boson interactions to enable teleported entangling operations between bosonic modes[45]. Although our work focuses on GKP states, these control strategies are adaptable to other bosonic codes, including rotation-symmetric codes[5], which may offer enhanced robustness against dephasing noise and exotic multimode grid state codes[46]. Finally, the high-fidelity spin–boson interactions demonstrated here could pave the way for emerging hybrid discrete- and continuous-variable QIP schemes[47], which have the potential to greatly advance quantum information science.

Online content

Any methods, additional references, Nature Portfolio reporting summaries, source data, extended data, supplementary information, acknowledgements, peer review information; details of author contributions and competing interests; and statements of data and code availability are available at https://doi.org/10.1038/s41567-025-03002-8.

References

1. Lloyd, S. & Braunstein, S. L. Quantum computation over continuous variables. *Phys. Rev. Lett.* **82**, 1784–1787 (1999).

2. Braunstein, S. L. & van Loock, P. Quantum information with continuous variables. *Rev. Mod. Phys.* **77**, 513–577 (2005).
3. Mirrahimi, M. et al. Dynamically protected cat-qubits: a new paradigm for universal quantum computation. *New J. Phys.* **16**, 045014 (2014).
4. Michael, M. H. et al. New class of quantum error-correcting codes for a bosonic mode. *Phys. Rev. X* **6**, 031006 (2016).
5. Grimsmo, A. L., Combes, J. & Baragiola, B. Q. Quantum computing with rotation-symmetric bosonic codes. *Phys. Rev. X* **10**, 011058 (2020).
6. Gottesman, D., Kitaev, A. & Preskill, J. Encoding a qubit in an oscillator. *Phys. Rev. A* **64**, 012310 (2001).
7. Albert, V. V. et al. Performance and structure of single-mode bosonic codes. *Phys. Rev. A* **97**, 032346 (2018).
8. Campagne-Ibarcq, P. et al. Quantum error correction of a qubit encoded in grid states of an oscillator. *Nature* **584**, 368–372 (2020).
9. Eickbusch, A. et al. Fast universal control of an oscillator with weak dispersive coupling to a qubit. *Nat. Phys.* **18**, 1464–1469 (2022).
10. Sivak, V. V. et al. Real-time quantum error correction beyond break-even. *Nature* **616**, 50–55 (2023).
11. Kudra, M. et al. Robust preparation of wigner-negative states with optimized snap-displacement sequences. *PRX Quantum* **3**, 030301 (2022).
12. Lachance-Quirion, D. et al. Autonomous quantum error correction of Gottesman-Kitaev-Preskill states. *Phys. Rev. Lett.* **132**, 150607 (2024).
13. Konno, S. et al. Logical states for fault-tolerant quantum computation with propagating light. *Science* **383**, 289–293 (2024).
14. Flühmann, C. et al. Encoding a qubit in a trapped-ion mechanical oscillator. *Nature* **566**, 513–517 (2019).
15. Neeve, B. D., Nguyen, T.-L., Behrle, T. & Home, J. P. Error correction of a logical grid state qubit by dissipative pumping. *Nat. Phys.* **18**, 296–300 (2022).
16. Matsos, V. G. et al. Robust and deterministic preparation of bosonic logical states in a trapped ion. *Phys. Rev. Lett.* **133**, 050602 (2024).
17. Royer, B., Singh, S. & Girvin, S. Stabilization of finite-energy Gottesman-Kitaev-Preskill states. *Phys. Rev. Lett.* **125**, 260509 (2020).
18. Hastrup, J. & Andersen, U. L. Improved readout of qubit-coupled Gottesman-Kitaev-Preskill states. *Quantum Sci. Technol.* **6**, 035016 (2021).
19. Rojkov, I. et al. Two-qubit operations for finite-energy Gottesman–Kitaev–Preskill encodings. *Phys. Rev. Lett.* **133**, 100601 (2024).
20. Barenco, A. et al. Elementary gates for quantum computation. *Phys. Rev. A* **52**, 3457–3467 (1995).
21. Bremner, M. J. et al. Practical scheme for quantum computation with any two-qubit entangling gate. *Phys. Rev. Lett.* **89**, 247902 (2002).
22. Raussendorf, R. & Briegel, H. J. A one-way quantum computer. *Phys. Rev. Lett.* **86**, 5188–5191 (2001).
23. Valahu, C. H. et al. Direct observation of geometric-phase interference in dynamics around a conical intersection. *Nat. Chem.* **15**, 1503–1508 (2023).
24. Tan, T. R. et al. Improving a trapped-ion quantum computer with a cryogenic sapphire oscillator. In *Joint Conference of the European Frequency and Time Forum and IEEE International Frequency Control Symposium (EFTF/IFCS)* (eds Weaver, G. et al.) 1–2 (IEEE, 2023).
25. Wineland, D. J. et al. Experimental issues in coherent quantum-state manipulation of trapped atomic ions. *J. Res. Natl Inst. Stand. Technol.* **103**, 259–328 (1998).
26. Sutherland, R. T. & Srinivas, R. Universal hybrid quantum computing in trapped ions. *Phys. Rev. A* **104**, 032609 (2021).
27. Ball, H. et al. Software tools for quantum control: improving quantum computer performance through noise and error suppression. *Quantum Sci. Technol.* **6**, 044011 (2021).
28. Horodecki, M., Horodecki, P. & Horodecki, R. General teleportation channel, singlet fraction, and quasidistillation. *Phys. Rev. A* **60**, 1888–1898 (1999).
29. Shaw, M. H., Doherty, A. C. & Grimsmo, A. L. Stabilizer subsystem decompositions for single- and multimode Gottesman-Kitaev-Preskill codes. *PRX Quantum* **5**, 010331 (2024).
30. Shaw, M. H., Doherty, A. C. & Grimsmo, A. L. Logical gates and read-out of superconducting Gottesman-Kitaev-Preskill qubits. Preprint at https://arxiv.org/abs/2403.02396 (2024).
31. Bourassa, J. E. et al. Blueprint for a scalable photonic fault-tolerant quantum computer. *Quantum* **5**, 392 (2021).
32. Kolesnikow, X. C., Bomantara, R. W., Doherty, A. C. & Grimsmo, A. L. Gottesman-Kitaev-Preskill state preparation using periodic driving. *Phys. Rev. Lett.* **132**, 130605 (2024).
33. Schäfer, V. M. et al. Fast quantum logic gates with trapped-ion qubits. *Nature* **555**, 75–78 (2018).
34. Chou, C.-W. et al. Preparation and coherent manipulation of pure quantum states of a single molecular ion. *Nature* **545**, 203–207 (2017).
35. Postler, L. et al. Demonstration of fault-tolerant universal quantum gate operations. *Nature* **605**, 675–680 (2022).
36. Chen, J.-S. et al. Benchmarking a trapped-ion quantum computer with 30 qubits. *Quantum* **8**, 1516 (2024).
37. Warring, U., Hakelberg, F., Kiefer, P., Wittemer, M. & Schaetz, T. Trapped ion architecture for multi-dimensional quantum simulations. *Adv. Quantum Technol.* **3**, 1900137 (2020).
38. Kiesenhofer, D. et al. Controlling two-dimensional Coulomb crystals of more than 100 ions in a monolithic radio-frequency trap. *PRX Quantum* **4**, 020317 (2023).
39. Guo, S.-A. et al. A site-resolved two-dimensional quantum simulator with hundreds of trapped ions. *Nature* **630**, 613–618 (2024).
40. Lysne, N. K., Niedermeyer, J. F., Wilson, A. C., Slichter, D. H. & Leibfried, D. Individual addressing and state readout of trapped ions utilizing radio-frequency micromotion. *Phys. Rev. Lett.* **133**, 033201 (2024).
41. Moses, S. et al. A race-track trapped-ion quantum processor. *Phys. Rev. X* **13**, 041052 (2023).
42. Jain, S. et al. Penning micro-trap for quantum computing. *Nature* **627**, 510–514 (2024).
43. Shaw, A. L. et al. Erasure-cooling, control, and hyper-entanglement of motion in optical tweezers. *Science* **388**, 845–849 (2025).
44. Hou, P.-Y. et al. Coherent coupling and non-destructive measurement of trapped-ion mechanical oscillators. *Nat. Phys.* **20**, 1636–1641 (2024).
45. Main, D. et al. Distributed quantum computing across an optical network link. *Nature* **638**, 383–388 (2025).
46. Royer, B., Singh, S. & Girvin, S. Encoding qubits in multimode grid states. *PRX Quantum* **3**, 010335 (2022).
47. Liu, Y. et al. Hybrid oscillator-qubit quantum processors: instruction set architectures, abstract machine models, and applications. Preprint at https://arxiv.org/abs/2407.10381 (2024).

Methods

GKP code

Here we give some background on GKP codes, highlighting some of the more salient features in our experiment and simulations. For a more comprehensive summary, see the original proposal[6] and more recent reviews[48,49]. The GKP code is a stabilizer code defined in a bosonic Hilbert space. Its stabilizer generators define a set of lattice points in phase space, which define the code. A family of GKP codes exists, each corresponding to a distinct lattice in phase space[46,50]. Here we focus on the square GKP code, which is the most fundamental qubit code in this family. The stabilizer generators for this code are given by the two commuting displacement operators

$$\hat{S}_X = \hat{D}(2\alpha), \quad \hat{S}_Z = \hat{D}(2\beta), \tag{2}$$

where $\beta = \mathrm{i}\alpha = \mathrm{i}\sqrt{\pi/2}$. These admit the following logical Pauli operators

$$\hat{X}_\mathrm{L} = \hat{D}(\alpha), \quad \hat{Y}_\mathrm{L} = \hat{D}(\alpha+\beta), \quad \hat{Z}_\mathrm{L} = \hat{D}(\beta), \tag{3}$$

which commute with the stabilizer generators. Furthermore, a logical $\mathrm{C}Z_\mathrm{L}$ gate takes the simple form

$$\hat{\mathrm{C}}Z_\mathrm{L} = \mathrm{e}^{\mathrm{i}\hat{q}_1\hat{q}_2}, \tag{4}$$

where $\hat{q}_j = (\hat{a}_j + \hat{a}_j^\dagger)/\sqrt{2}$ denotes the position operator for mode j.

The code words, which are defined to be the ±1 eigenstates of the stabilizer generators in equation (2), may be expressed in phase space as an infinite sum of coherent states localized at the lattice points defined by α and β:

$$\begin{aligned} |+Z_\mathrm{L}^\mathrm{ideal}\rangle &= \sum_{k,l=-\infty}^{\infty} \mathrm{e}^{-\mathrm{i}\pi kl} |2k\alpha + l\beta\rangle_\mathrm{c}, \\ |-Z_\mathrm{L}^\mathrm{ideal}\rangle &= \sum_{k,l=-\infty}^{\infty} \mathrm{e}^{-\mathrm{i}\pi(kl+l/2)} |(2k+1)\alpha + l\beta\rangle_\mathrm{c}, \end{aligned} \tag{5}$$

where $|\gamma\rangle_\mathrm{c} = \hat{D}(\gamma)|0\rangle$ is a coherent state and $|0\rangle$ is the vacuum state. These states are the ±1 eigenstates of Z_L, and similar expressions for the ±1 eigenstates of the other logical Pauli operators, $|\pm X_\mathrm{L}^\mathrm{ideal}\rangle$ $|\pm Y_\mathrm{L}^\mathrm{ideal}\rangle$, may be obtained by taking superpositions of these states.

Owing to their infinite extent in phase space, these code words have infinite energy. Finite-energy GKP states may be defined by applying the envelope operator onto the infinite energy code words:

$$|\pm P_\mathrm{L}\rangle = \frac{\mathrm{e}^{-\Delta^2 a^\dagger a}}{\mathcal{N}} |\pm P_\mathrm{L}^\mathrm{ideal}\rangle, \tag{6}$$

where $P = X, Y, Z$, and $\mathcal{N} = \sqrt{\langle \pm P_\mathrm{L}^\mathrm{ideal}| \mathrm{e}^{-2\Delta^2 a^\dagger a} |\pm P_\mathrm{L}^\mathrm{ideal}\rangle}$. These are approximate ±1 eigenstates of the stabilizer generators and $\Delta \in [0, 1]$ parameterizes this approximation, with $\Delta \to 0$ recovering the infinite energy code words. Crucially, the logical operators in equation (3) are not exact logical operators for the finite-energy code words. Methods to construct logical operators that are exact for finite-energy code words via the envelope operator, for example, $\mathrm{e}^{-\Delta^2 \hat{a}^\dagger \hat{a}} \hat{Z}_\mathrm{L} \mathrm{e}^{\Delta^2 \hat{a}^\dagger \hat{a}}$, have been explored for SQ gates in ref. 17 and for the $\mathrm{C}Z_\mathrm{L}$ gate in ref. 19.

We stress that the construction for finite-energy GKP states in equation (6) is not unique, and that the exact form of the approximation will depend on the details of the experimental platform that the states are prepared in. This motivates our use of an optimizer to find a logical operation that is tailored to the exact form of the approximate GKP states. However, for numerical purposes, we find an alternative definition for the finite-energy GKP code, which was used in refs. 32,51, particularly useful. Here the code states are defined to be the quasidegenerate ground states of the Hamiltonian

$$\hat{H}_\mathrm{GKP} = \omega_0 \hat{a}^\dagger \hat{a} - J(\cos(2\sqrt{\pi}\hat{q}) + \cos(2\sqrt{\pi}\hat{p})), \tag{7}$$

where $\hat{q} = (\hat{a} + \hat{a}^\dagger)/\sqrt{2}$ and $\hat{p} = -\mathrm{i}(\hat{a} - \hat{a}^\dagger)/\sqrt{2}$ are the position and momentum operators for a single bosonic mode, respectively; ω_0 represents the characteristic energy scale of the harmonic oscillator; and J quantifies the stabilizer potential enforcing the periodic structure of the GKP code. In the limit of large J/ω_0, the ground states are approximately logical Hadamard eigenstates in the $|+Z_\mathrm{L}\rangle$ basis,

$$|+H_\mathrm{L}\rangle = \cos(\pi/8)|+Z_\mathrm{L}\rangle + \sin(\pi/8)|-Z_\mathrm{L}\rangle, \tag{8a}$$

$$|-H_\mathrm{L}\rangle = -\sin(\pi/8)|+Z_\mathrm{L}\rangle + \cos(\pi/8)|-Z_\mathrm{L}\rangle, \tag{8b}$$

and the squeezing parameter Δ of these states is related to the energy scales through $\Delta = (\omega_0/(4\pi J))^{1/4}$. We find numerical diagonalization of equation (7) to be an efficient procedure to obtain the finite-energy GKP code words numerically. The relations in equation (8) may be inverted to obtain the $|+Z_\mathrm{L}\rangle$ code words, and the other logical Pauli eigenstates obtained from the appropriate superpositions of these states.

Furthermore, the squeezing parameter of these states in each quadrature $\Delta_{X/Z}$ may be independently calculated from their stabilizer expectation values through the relations[52]

$$\Delta_X = \sqrt{-\frac{1}{2\pi}\log\left[|\langle \hat{S}_X\rangle|^2\right]}, \tag{9a}$$

$$\Delta_Z = \sqrt{-\frac{1}{2\pi}\log\left[|\langle \hat{S}_Z\rangle|^2\right]}, \tag{9b}$$

which can also be expressed in units of decibels, with $\Delta_{X/Z}\,(\mathrm{dB}) = -10\log_{10}[\Delta_{X/Z}^2]$. In this work, we set $J/\omega_0 = 5.95$ in equation (7) to target logical states $\{|+Z_\mathrm{L}\rangle, |-Z_\mathrm{L}\rangle, |+X_\mathrm{L}\rangle, |+Y_\mathrm{L}\rangle\}$ with squeezing parameters $[\Delta_X, \Delta_Z]$ of {[8.39, 7.90], [8.36, 8.88], [7.90, 8.39], [8.38, 8.38]} dB, respectively.

Logical measurements on the GKP code using SSSD

SSSD provides a way to divide the infinite-dimensional Hilbert space into a logical subsystem, containing the logical information encoding in a GKP state, and a gauge subsystem, referred to as the stabilizer subsystem[29,53]. Here we make use of this formalism to accurately and efficiently readout the logical information encoded in our states.

Logical readout for the ideal square GKP code corresponds to measuring the expectation values of the logical Pauli operators, $\{\langle \hat{X}_\mathrm{L}\rangle, \langle \hat{Y}_\mathrm{L}\rangle, \langle \hat{Z}_\mathrm{L}\rangle\}$. The expectation values of these logical Pauli operators are obtained by applying an SDF interaction, which transfers information from the bosonic mode to the ancilla, followed by an ancilla measurement. Setting the phases ϕ_s and ϕ_m to be time independent with $\phi_\mathrm{s} = 0$, the application of the SDF interaction from equation (1) for a time t realizes the operation $\hat{D}(\gamma\hat{\sigma}_x/2)$, where $\gamma = -\mathrm{i}\Omega t \mathrm{e}^{-\mathrm{i}\phi_\mathrm{m}}$. The magnitude of displacement, $|\gamma|$, is controlled by the duration of the SDF pulse, t, and the phase of the displacement, $\arg(\gamma)$, is controlled by the SDF phase, ϕ_m. Following the SDF pulse, the state measurement of the ancilla gives $\langle \hat{\sigma}_z\rangle = \mathrm{Re}[\langle \hat{D}(\gamma(t, \phi_\mathrm{m}))\rangle]$, whereas the imaginary part can be obtained by applying an ancilla qubit rotation before the SDF. Setting $\gamma = \{\alpha, \alpha+\beta, \beta\}$ leads to the measurements of $\{\langle \hat{X}_\mathrm{L}\rangle, \langle \hat{Y}_\mathrm{L}\rangle, \langle \hat{Z}_\mathrm{L}\rangle\}$.

The expectation value of joint Pauli logical operators on two bosonic modes is obtained by applying two sequential SDF operations followed by an ancilla measurement, resulting in $\mathrm{Re}\,[\langle \hat{D}(\gamma) \otimes \hat{D}(\delta)\rangle]$.

To decode a GKP state, measuring the Pauli expectation values of finite-energy GKP states with the operators of equation (3) is only valid in the limit $\Delta \to 0$. As explained in the main text, one can instead measure the expectation value of the Pauli measurement operators, which was done for the SQ gates and Bell state characterization. These operators are defined as a summation over displacement operators on the logical GKP lattice[30]:

$$\hat{X}_\mathrm{m} = \frac{1}{\pi} \sum_{n=-N}^{N-1} \frac{(-1)^n}{n + \frac{1}{2}} \hat{D}(\alpha(2n+1)), \tag{10a}$$

$$\hat{Y}_{\mathrm{m}} = \frac{1}{\pi^2}\sum_{m,n=-N}^{N-1}\frac{\hat{D}\left(\alpha(2n+1)+\beta(2m+1)\right)}{\left(n+\frac{1}{2}\right)\left(m+\frac{1}{2}\right)}, \tag{10b}$$

$$\hat{Z}_{\mathrm{m}} = \frac{1}{\pi}\sum_{m=-N}^{N-1}\frac{(-1)^m}{m+\frac{1}{2}}\hat{D}\left(\beta(2m+1)\right), \tag{10c}$$

where N sets a truncation, and the identity Pauli measurement operator $\hat{I}_{\mathrm{m}}$ coincides with the identity operator on Fock space. The expectation values $\langle\hat{X}_{\mathrm{m}}\rangle$, $\langle\hat{Y}_{\mathrm{m}}\rangle$ and $\langle\hat{Z}_{\mathrm{m}}\rangle$ are obtained by summing over the expectation values of the displacement operator, $\langle\hat{D}(\gamma)\rangle$. Here γ is varied to sample the various points determined by equation (10). Expectations of joint Pauli measurement operators for two bosonic modes, such as $\langle\hat{X}_{\mathrm{m}}\otimes\hat{Z}_{\mathrm{m}}\rangle$, can be obtained by taking the tensor product of any two single-mode Pauli measurement operator of equation (10). Their joint expectation value will also be a summation over the expectation values of two-mode displacement operators.

The number of required measurements is reduced by using the fact that $\langle\hat{D}(\gamma)\rangle = \langle\hat{D}(-\gamma)\rangle^*$. With this, the total number of measurements to calculate the three single-mode expectation values of the Pauli measurement operators of equation (10) is $N_{\mathrm{meas}} = 2N + 2N^2$. For the expectation values of the 15 non-trivial two-mode Pauli measurement operators, the number of measurements is $N_{\mathrm{meas}} = 4N + 8N^2 + 8N^3 + 4N^4$. The finite-energy envelope of the GKP states implies that $\langle\hat{D}(\gamma)\rangle \approx 0$ for large enough $|\gamma|$, meaning that the sums in equation (10) converge with N. In both SQ gate and Bell state experiments, we choose a truncation of $N = 2$ to minimize the number of measurements required, but still achieve a good approximation (in Supplementary Section C, we quantify the error arising from this truncation). This results in $N_{\mathrm{meas}} = 12$ and $N_{\mathrm{meas}} = 168$ measurements for logical SQ and TQ states, respectively. For the CZ_{L} gate experiment, we choose not to measure the Pauli measurement operators because the required number of measurements for all 16 states is 2,688, leading to a much longer experimental runtime. Instead, we choose to measure the expectation values of the logical Pauli operators of equation (3), which requires a total of 240 measurements, and incorporate the error from using these operators into our error budget (Supplementary Fig. 3).

State tomography

In the SQ experiment, the logical density matrices $\hat{\rho}_{\mathrm{L}}^{\mathrm{in}}$ and $\hat{\rho}_{\mathrm{L}}^{\mathrm{out}}$ are reconstructed from the Pauli measurement expectation values using the relation

$$\hat{\rho}_{\mathrm{L}} = \frac{1}{2}\hat{E}^0 + \frac{1}{2}\sum_{i=1}^{3}\left\langle\hat{E}_{\mathrm{m}}^i\right\rangle\hat{E}^i, \tag{11}$$

where $\hat{E}^i \in \{\hat{I}, \hat{\sigma}_x, \hat{\sigma}_y, \hat{\sigma}_z\}$ are the usual one-qubit Pauli operators and $\hat{E}_{\mathrm{m}}^i \in \{\hat{I}_{\mathrm{m}}, \hat{X}_{\mathrm{m}}, \hat{Y}_{\mathrm{m}}, \hat{Z}_{\mathrm{m}}\}$ are the Pauli measurement operators, which can be obtained from the experiment using equation (10). We construct a tomographically complete set of $\hat{\rho}_{\mathrm{L}}^{\mathrm{in}}$ by preparing one of the four states $\{|+Z_{\mathrm{L}}\rangle, |-Z_{\mathrm{L}}\rangle, |+X_{\mathrm{L}}\rangle, |+Y_{\mathrm{L}}\rangle\}$ and taking measurements for each of the expectation values in equation (11), leading to a total of $4 \times 12 = 48$ measurements (Supplementary Section B). Reconstructing each $\hat{\rho}_{\mathrm{L}}^{\mathrm{out}}$ is performed in a similar manner, but with the gate applied to each initial state.

In the TQ experiment, the input and output density matrices are reconstructed from Pauli expectation values using the relation

$$\hat{\rho}_{\mathrm{L}} = \frac{1}{4}\hat{E}^0 + \frac{1}{4}\sum_{i=1}^{15}\langle\hat{E}_{\mathrm{L}}^i\rangle\hat{E}^i, \tag{12}$$

where $\hat{E}^i \in \{\hat{I}, \hat{\sigma}_x, \hat{\sigma}_y, \hat{\sigma}_z\}^{\otimes 2}$ are the TQ Pauli operators and $\hat{E}_{\mathrm{L}}^i \in \{\hat{I}_{\mathrm{L}}, \hat{X}_{\mathrm{L}}, \hat{Y}_{\mathrm{L}}, \hat{Z}_{\mathrm{L}}\}^{\otimes 2}$ are the logical Pauli operators of equation (3). We first reconstruct each $\hat{\rho}_{\mathrm{L}}^{\mathrm{in}}$ by preparing one of the 16 possible input states from the set $\{|+Z_{\mathrm{L}}\rangle, |-Z_{\mathrm{L}}\rangle, |+X_{\mathrm{L}}\rangle, |+Y_{\mathrm{L}}\rangle\}^{\otimes 2}$ and measuring the 15 different non-trivial logical Pauli operators, resulting in $16 \times 15 = 240$ measurements. Similarly, each $\hat{\rho}_{\mathrm{L}}^{\mathrm{out}}$ is retrieved by applying the CZ_{L} gate after preparing one of the input states.

The Bell state is characterized using logical QST, which aims to reconstruct the logical density matrix of the experimentally prepared state. In the Bell state experiment, we reconstruct the logical density matrix from

$$\hat{\rho}_{\mathrm{L}} = \frac{1}{4}\hat{E}^0 + \frac{1}{4}\sum_{i=1}^{15}\langle\hat{E}_{\mathrm{m}}^i\rangle\hat{E}^i, \tag{13}$$

where $\hat{E}^i \in \{\hat{I}, \hat{\sigma}_x, \hat{\sigma}_y, \hat{\sigma}_z\}^{\otimes 2}$ are the TQ Pauli operators and $\hat{E}_{\mathrm{m}}^i \in \{\hat{I}_{\mathrm{m}}, \hat{X}_{\mathrm{m}}, \hat{Y}_{\mathrm{m}}, \hat{Z}_{\mathrm{m}}\}^{\otimes 2}$ are the Pauli measurement operators. The expectation values are calculated from equation (10), where a truncation of $N = 2$ results in 168 unique measurements. We apply a post-processing step in the logical Bell state analysis, ensuring that the reconstructed state is physical. After obtaining $\hat{\rho}_{\mathrm{L}}$ from equation (13), we use a convex optimizer to obtain a physical density matrix, $\hat{\rho}_{\mathrm{L,Bell}}$, which minimizes $||\hat{\rho}_{\mathrm{L,Bell}} - \hat{\rho}_{\mathrm{L}}||_2$ (ref. 54). $\hat{\rho}_{\mathrm{L,Bell}}$ is constrained to be non-negative definite and $\mathrm{Tr}\,(\hat{\rho}_{\mathrm{L,Bell}}) = 1$. Expectation values of the physical density matrix $\hat{\rho}_{\mathrm{L,Bell}}$ are plotted in Fig. 4.

Uncertainty analysis

Uncertainties on the logical fidelities presented in this work are determined using a non-parametric bootstrap procedure. For each dataset, we resample the raw spin readout counts with replacement to create 1,000 pseudo-datasets of identical size. Each resampled dataset is processed through the full analysis: first extracting the relevant displacement operator expectation values, then reconstructing the logical density matrix or process matrix and finally calculating the fidelity metric. The standard deviation of the resulting distribution of 1,000 fidelity values is taken as the one standard deviation (1σ) statistical uncertainty reported in the main text.

Calibration and experimental drift

To mitigate errors from slow experimental drifts, we implement an interleaved calibration routine throughout the experiment. The motional mode frequencies ω_x and ω_y, corresponding to the radial-x and radial-y modes, are periodically recalibrated approximately every 30 s using a calibration protocol described in ref. 55. Independent measurements reveal that the frequency drifts by $\sigma_\delta \approx 2\pi \times 3.2$ Hz between calibrations, and that drifts in ω_x and ω_y are highly correlated. We estimate errors due to frequency drifts from numerical simulations by repeating a similar analysis, as carried out in Supplementary Section C. The SDF Hamiltonian in equation (1) is modified by adding a noisy Hamiltonian term of the form $\delta_x\hat{a}_1^\dagger\hat{a}_1 + \delta_y\hat{a}_2^\dagger\hat{a}_2$. We set $\delta = \delta_x = \delta_y$ to model-correlated frequency drifts, and $\delta \approx \mathcal{N}(0, \sigma_\delta^2)$ is sampled from a normal distribution. The resulting infidelity is below 5×10^{-3} across all experiments.

By contrast, drifts in the qubit frequency and SDF Rabi rate occur on much slower timescales and are not included in the scheduled calibration routine. These parameters do not appreciably drift over the duration of the experiments and have a negligible impact on the fidelities relative to drifts in the motional frequency.

Data availability

The experimental data are available via Zenodo at https://doi.org/10.5281/zenodo.13940370 (ref. 56). Source data are provided with this paper.

References

48. Grimsmo, A. L. & Puri, S. Quantum error correction with the Gottesman-Kitaev-Preskill code. *PRX Quantum* **2**, 020101 (2021).

49. Brady, A. J., Eickbusch, A., Singh, S., Wu, J. & Zhuang, Q. Advances in bosonic quantum error correction with Gottesman-Kitaev-Preskill codes: theory, engineering and applications. *Prog. Quantum Electron.* **93**, 100496 (2024).
50. Conrad, J., Eisert, J. & Arzani, F. Gottesman-Kitaev-Preskill codes: a lattice perspective. *Quantum* **6**, 648 (2022).
51. Rymarz, M., Bosco, S., Ciani, A. & DiVincenzo, D. P. Hardware-encoding grid states in a nonreciprocal superconducting circuit. *Phys. Rev. X* **11**, 011032 (2021).
52. Duivenvoorden, K., Terhal, B. M. & Weigand, D. Single-mode displacement sensor. *Phys. Rev. A* **95**, 012305 (2017).
53. Pantaleoni, G., Baragiola, B. Q. & Menicucci, N. C. Modular bosonic subsystem codes. *Phys. Rev. Lett.* **125**, 040501 (2020).
54. Riofrío, C. A. et al. Experimental quantum compressed sensing for a seven-qubit system. *Nat. Commun.* **8**, 15305 (2017).
55. MacDonell, R. J. et al. Predicting molecular vibronic spectra using time-domain analog quantum simulation. *Chem. Sci.* **14**, 9439–9451 (2023).
56. Matsos, V. G. et al. Universal quantum gate set for Gottesman-Kitaev-Preskill logical qubits. *Zenodo* https://doi.org/10.5281/zenodo.13940370 (2025).

Acknowledgements

We thank B. Baragiola, N. Mennicucci, M. Stafford, Z. Huang, T. Smith and R. Harper for fruitful discussions. We were supported by the Australian Research Council (FT220100359), the Sydney Horizon Fellowship (T.R.T.), the US Office of Naval Research Global (N62909-24-1-2083), the US Army Research Office Laboratory for Physical Sciences (W911NF-21-1-0003), the US Air Force Office of Scientific Research (FA2386-23-1-4062), Lockheed Martin, the Sydney Quantum Academy (M.J.M.), the University of Sydney Postgraduate Award scholarship (V.G.M.), the Australian Government Research Training Program scholarship (X.C.K.), H. Harley and A. Harley.

Author contributions

V.G.M., C.H.V. and T.R.T. conceived the idea. V.G.M. developed the SDF numerical optimization, performed the experiment and analysed the data. V.G.M., C.H.V., M.J.M., T.R.T. and T.N. contributed to the experimental apparatus, and X.C.K. provided theoretical support. T.R.T. supervised the project. V.G.M., C.H.V., M.J.B. and T.R.T. wrote the paper. All authors provided suggestions for the experiment, discussed the results and contributed to the paper.

Funding

Open access funding provided by the University of Sydney.

Competing interests

The authors declare no competing interests.

Additional information

Supplementary information The online version contains supplementary material available at https://doi.org/10.1038/s41567-025-03002-8.

Correspondence and requests for materials should be addressed to V. G. Matsos or T. R. Tan.

Peer review information *Nature Physics* thanks the anonymous reviewers for their contribution to the peer review of this work.